• Original Paper •

Insights into the Microwave Instruments Onboard the Fengyun 3D Satellite: Data Quality and Assimilation in the Met Office NWP System

Fabien CARMINATI[*1], Nigel ATKINSON[1], Brett CANDY[1], and Qifeng LU[2]

[1]*Met Office*, *Exeter EX*1 3*PB*, *UK*

[2]*National Satellite Meteorological Center*, *China Meteorological Administration*, *Beijing* 100081, *China*

ABSTRACT

This paper evaluates the microwave instruments onboard the latest Chinese polar-orbiting satellite, Fengyun 3D (FY-3D). Comparing three months of observations from the Microwave Temperature Sounder 2 (MWTS-2), the Microwave Humidity Sounder 2 (MWHS-2), and the Microwave Radiation Imager (MWRI) to Met Office short-range forecasts, we characterize the instrumental biases, show how those biases have changed with respect to their predecessors onboard FY-3C, and how they compare to the Advanced Technology Microwave Sounder (ATMS) onboard NOAA-20 and the Global Precipitation Measurement Microwave Imager (GMI). The MWTS-2 global bias is much reduced with respect to its predecessor and compares well to ATMS at equivalent channel frequencies, differing only by 0.36 ± 0.28 K (1σ) on average. A suboptimal averaging of raw digital counts is found to cause an increase in striping noise and an ascending—descending bias. MWHS-2 benefits from a new calibration method improving the 183-GHz humidity channels with respect to its predecessor and biases for these channels are within $\pm$ 1.9 K to ATMS. MWRI presents the largest improvements, with reduced global bias and standard deviation with respect to FY-3C; although, spurious, seemingly transient, brightness temperatures have been detected in the observations at 36.5 GHz (vertical polarization). The strong solar-dependent bias that affects the instrument on FY-3C has been reduced to less than 0.2 K on average for FY-3D MWRI. Experiments where radiances from these instruments were assimilated on top of a full global system demonstrated a neutral to positive impact on the forecasts, as well as on the fit to the background of independent instruments.

Key words: microwave remote sensing, numerical weather prediction, data assimilation

Article Highlights:

- MWTS-2 global bias is reduced with respect to its predecessor and compares well to the reference U.S. instruments, although it is noisier.
- MWHS-2 benefits from a new calibration improving the 183-GHz channels, with a noise comparable to the reference U.S. instrument.
- MWRI has reduced global bias and noise with respect to its predecessor, but with spurious transient brightness temperatures in one channel.
- Assimilation of FY-3D microwave radiances in the Met Office NWP system has a neutral to positive impact on forecasts.

---

1. Introduction

Satellite microwave instruments have contributed to the Earth observing system for decades, providing key observations for numerical weather prediction (NWP), re-analyses, and climate data records (e.g., English et al., 2000; Uppala

et al., 2005; Yang et al., 2016a). Arguably of foremost importance, the assimilation of temperature and humidity-sensitive microwave radiances, and wind-derived information, have continuously driven the quality of weather forecasts at the Met Office and other NWP centers (Joo et al., 2013; Kazumori et al., 2016), leading to improved societal benefits and resilience to extreme weather events (Pielke and Carbone, 2002; Bauer et al., 2015).

Since the 1980s, China has developed extensive Earth

---

* Corresponding author: Fabien CARMINATI
  Email: fabien.carminati@metoffice.gov.uk

observation satellite programs dedicated to meteorology, oceanography, and Earth surface monitoring (Gu and Tong, 2015), catching up in a field long dominated by the U.S. and Europe. The Fengyun 3 (FY-3) program is of particular interest to NWP centers. To date, two research (FY-3A and B) and two operational (FY-3C and D) platforms have been launched, and four more are scheduled in the coming years (Yang et al., 2011). Note that FY-3A ceased operations in March 2018. The equator crossing time (ECT) is 1400 ECT on the ascending node for FY-3D, 1015 ECT on the descending node for FY-3C, and 1338 ECT on the ascending node for FY-3B.

In this study, we focus on the Microwave Temperature Sounder 2 (MWTS-2) and the Microwave Humidity Sounder 2 (MWHS-2) instruments, first introduced as part of the FY-3C payload and continued on FY-3D, as well as the Microwave Radiation Imager (MWRI) that has been part of the payload of all FY-3 platforms to date. Together, these instruments have radiometric capability spanning the microwave domain from 10 to 183 GHz and provide valuable information on temperature, humidity and wind.

To date and to the best of our knowledge, only the China Meteorological Administration (CMA), Météo-France, the European Centre for Medium-Range Weather Forecasts (ECMWF), the Indian National Centre for Medium Range Weather Forecasting, and the Met Office are operationally using observations from the microwave instruments onboard the FY-3 constellation, although other major NWP centers are planning to investigate the use of those data.

Following the FY-3C power fault in May 2015 and the subsequent failure of MWTS-2, the instrument has never been used for operational purposes. However, Li and Liu (2016) have reported neutral to slightly positive impacts on analyses and forecasts from a series of observing system experiments in GRAPES (the CMA's Global and Regional Assimilation and Prediction System).

Observations from FY-3C MWHS-2 (and its less-advanced predecessor FY-3B MWHS-1) have been assimilated in operations at the Met Office and ECMWF since 2016 (Chen et al., 2015, 2018; Carminati et al., 2018, Lawrence et al., 2018), noting that at ECMWF, 118 and 183 GHz channels are assimilated in the all-sky framework, while only low scattering scenes at 183 GHz are used at the Met Office. The impact was reported to be neutral to slightly positive at both centers. At the Met Office, MWHS-1 and MWHS-2 contributed to the total percentage impact on 24-h forecast error reduction by 0.8% and 1.5%, respectively, as of December 2018.

There is no published report of an operational use of FY-3C MWRI, although observing system experiments carried out at the Met Office have demonstrated a reduction of the forecast root-mean-square errors (RMSEs) from T+0 to T+144 (6 days) of 0.16% and 0.15% with respect to conventional observations and ECMWF analyses, respectively. The assimilation of MWRI observations in the Met Office

operational system started in December 2019.

The microwave instruments onboard FY-3D, the latest platform of the series, launched on 14 November 2017, are therefore expected to further improve and increase the resilience of operational NWP systems. Following a successful post-launch test phase, the CMA has since mid-June 2019 been distributing observations from FY-3D MWTS-2, MWHS-2 and MWRI via EUMETSAT's dissemination system, EUMETCast (https://www.eumetsat.int/website/home/Data/DataDelivery/EUMETCast/index.html, last accessed on March 06, 2020). In line with the international effort to evaluate and optimize the use of data from the FY-3 program for NWP applications, we have been investigating the data quality between 15 June and 15 September 2019.

The post-launch data quality characterization of a new instrument is multifaceted. Diverse complementary methods have been devised to this end, such as comparisons with conventional observations from dedicated field campaigns or permanent sites (Bobak et al, 2005; Macelloni et al., 2006), calibrations against invariant targets (Burgdorf et al., 2016; Yang et al., 2016b, 2018), or inter-satellite cross validation (Zou and Wang, 2011; Moradi et al., 2015; Berg et al., 2016). The strict collocation criteria required by these approaches tend, however, to limit the temporal and spatial extent of the sampling (e.g., Cao et al., 2004).

In parallel in the NWP community, it has become common practice to evaluate satellite observations against forecasts, analyses, and reanalyses. This type of assessment has found a growing resonance with the improvement of model accuracy (Bauer et al., 2015), which enables the detection of calibration errors, radiometer nonlinearity, shifts in channel frequency, or solar thermal induced biases (Bormann et al., 2013; Saunders et al., 2013; Newman et al., 2020).

The continuous, global and homogeneous representation of atmospheric temperature and humidity fields offered by NWP models is an advantage for the evaluation of satellite observations. The optimal state of the atmosphere is estimated by the underlying data assimilation system that uses a short-range forecast adjusted, under the constraints of the model physics, by the information derived from millions of observations. To diagnose observational datasets, a radiative transfer model is used to simulate top-of-atmosphere brightness temperatures from the NWP model fields at frequencies used by satellite instruments. This method, referred to as the forward model, is generally preferred to comparisons in the model geophysical space that requires the computation of satellite retrieval profiles, whose solution can derive from multiple atmospheric states (Rodgers, 2000).

Biases and uncertainties present in the model fields, in the radiative transfer modeling, or caused by scale mismatch, are a limitation to the characterization of biases in satellite observations. Nevertheless, recent work indicates that the NWP framework remains suitable for the evaluation of instruments whose radiometric uncertainty is of the order of a few tenths of a Kelvin (Newman et al., 2020). Addi-

tionally, the use of double differences can alleviate the potential problem of NWP model biases. This approach consists of indirect comparisons of two sets of observations through comparisons with the model, hence cancelling out the effect of biases in the model to only reflect biases in the datasets that are being compared.

The assessment proposed in this study is based on the comparison of FY-3D instruments with short-range forecasts from the Met Office global model, their FY-3C predecessors, the Advanced Technology Microwave Sounder (ATMS) and the Global Precipitation Measurement (GPM) Microwave Imager (GMI).

This paper is structured as follows: section 2 presents the instrument characteristics; the data quality is discussed in section 3; section 4 presents the outputs of assimilation experiments; section 5 concludes the study.

2. Instrument characteristics

MWHS-2 is a 15-channel cross-track radiometer scanning a 2660-km swath in 98 steps at ± 53.35° from nadir. Its sounding capability covers the oxygen band at 118 GHz with a sub-satellite point resolution of 32 km, the water vapor band at 183 GHz with a 16-km resolution, and window parts of the spectrum at 89 and 150 GHz with a 32-km resolution. The five channels dedicated to the 183-GHz band and sensitive to humidity, cloud and precipitation, are similar although not identical to those of ATMS onboard the NOAA SNPP and NOAA-20 platforms. Unlike other operational spaceborne radiometers, MWHS-2 also provides a unique insight into the 118-GHz oxygen band. While the three highest peaking channels near the band center act as stratospheric temperature sounding channels, the sensitivity to cloud and precipitation—due to absorption, emission and scattering from hydrometeors—increases with the distance to

the band center as the channels peak lower in the troposphere. Lawrence et al. (2017) showed that, towards the edges of the band (at 118.75 ± 2.5 GHz), the absorption from the water vapor continuum is important compared to the absorption from dioxygen molecules in a dry atmosphere, which causes this channel to also be sensitive to water vapor. Finally, the two channels sounding the outermost edges of the band act as window channels with sensitivity to surface properties and water vapor. As noted by Lu et al. (2015), there is a disagreement between the polarization documented by the instrument manufacturer and the that derived from comparisons with NWP fields. In this study, we use the polarization defined in the official RTTOV radiative transfer coefficients (https://www.nwpsaf.eu/site/software/rttov/download/coefficients/detailed-file-history/#mw_fy3_mwhs2; last accessed 11 March 2020) as recommended by Lu et al. (2015). MWHS-2 characteristics are further detailed by He et al. (2015), and Table 1 summarizes the channel specifications along with the humidity sounding channels of ATMS.

MWTS-2, a 13-channel cross-track radiometer, covers a 2250-km swath in 90 steps with a sub-satellite point resolution of 32 km. In terms of radiometric capability, MWTS-2 sounds the oxygen band between 50 and 60 GHz with sensitivity to temperature from the surface to the upper stratosphere. MWTS-2 channels present similar characteristics to ATMS temperature-sensitive channels. The instrument is further detailed by Wang and Li (2014), and Table 2 summarizes the channel specifications along with ATMS equivalent channels.

MWRI is a conical-scanning radiometer with an antenna diameter of 90 cm that provides Earth observations at a viewing angle of 53.1° in the forward direction, with an azimuth range ± 52° for a total swath of 1400 km. In terms of radiometric capability, MWRI has 10 channels with dual

Table 1. MWHS-2 and ATMS channel number, central frequency and polarization, bandwidth, and horizontal resolution.

Channel number		Central frequency (GHz) & polarization		Bandwidth (MHz)		Horizontal resolution (km)	
MWHS2	ATMS	MWHS2	ATMS	MWHS2	ATMS	MWHS2	ATMS
1	16	89.0 QH	88.2 QV	1500	2000	32	32
2	–	118.75 ± 0.08 QV	–	20	–	32	–
3	–	118.75 ± 0.2 QV	–	100	–	32	–
4	–	118.75 ± 0.3 QV	–	165	–	32	–
5	–	118.75 ± 0.8 QV	–	200	–	32	–
6	–	118.75 ± 1.1 QV	–	200	–	32	–
7	–	118.75 ± 2.5 QV	–	200	–	32	–
8	–	118.75 ± 3.0 QV	–	1000	–	32	–
9	–	118.75 ± 5.0 QV	–	2000	–	32	–
10	17	150 QH	165.5 QH	1500	3000	16	16
11	22	183.31 ± 1 QV	183.31 ± 1 QH	500	500	16	16
12	21	183.31 ± 1.8 QV	183.31 ± 1.8 QH	700	1000	16	16
13	20	183.31 ± 3.0 QV	183.31 ± 3.0 QH	1000	1000	16	16
14	19	183.31 ± 4.5 QV	183.31 ± 4.5 QH	2000	2000	16	16
15	18	183.31 ± 7.0 QV	183.31 ± 7.0 QH	2000	2000	16	16

Notes: QV, quasi-vertical; QH, quasi-horizontal (i.e., polarization vector is parallel to the scan plane at nadir).

polarization at 10.65, 18.7, 23.8, 36.5 and 89.0 GHz. The spatial resolution ranges from 9 to 85 km, increasing with the decrease in frequency. The instrument is sensitive to surface thermal microwave emission and provides information on total column water vapor, cloud and precipitation, surface temperature, and surface wind over the ocean. MWRI benefits from an end-to-end three-point calibration system involving three reflectors: a main reflector used for the Earth, cold and warm views, and two independent reflectors used for the cold and warm targets exclusively. This system allows for the emission contamination from the sun-heated main reflector in the onboard calibration to be accounted for. MWRI characteristics, calibration system, and on-orbit performances are further discussed by Yang et al. (2011), noting that the authors address on-orbit performance of the instrument on FY-3A. MWRI shares frequencies with other imagers, including GMP GMI, a state-of-the-art conical-scanning radiometer, which, according to NASA, has achieved the highest standards of radiometric calibration and stability to date. Note that because the orbit pattern and antenna size (1.2 m) are different, GMI ground resolution [see, for example, Newell et al. (2014)] differs from MWRI. Table 3 summarizes MWRI and GMI channel specifications.

3. Assessment

Upon receipt, the data are pre-processed with the ATOVS and AVHRR Preprocessing Package (https://nwpsaf.eu/site/software/aapp/; last accessed 6 March 2020), converted to BUFR format, and stored in the Met Office observational database ready for use in the system. The pre-processing of MWHS-2 and MWTS-2 is a two-step process, similar to what was initially set up for FY-3C. First, each three adjacent scan positions are averaged to avoid oversampling. Second, MWHS-2 is mapped to MWTS-2 observations with a median filter in brightness temperature that is applied to any MWHS-2 spots within 1.25° (in viewing angle) of each

Table 2. As in Table 1 but for MWTS-2.

Channel number		Central frequency (GHz) & polarization		Bandwidth (MHz)		Horizontal resolution (km)	
MWTS2	ATMS	MWTS2	ATMS	MWTS2	ATMS	MWTS2	ATMS
1	3	50.30 QH	50.30 QH	180	180	32	32
2	4	51.76 QH	51.76 QH	400	400	32	32
3	5	52.80 QH	52.80 QH	400	400	32	32
4	6	53.596 ± 0.115 QH	53.596 ± 0.115 QH	400	170	32	32
5	7	54.40 QH	54.40 QH	400	400	32	32
6	8	54.94 QH	54.94 QH	400	400	32	32
7	9	55.50 QH	55.50 QH	330	330	32	32
8	10	57.29 QH	57.29 QH	330	155	32	32
9	11	57.29 ± 0.217 QH	57.29 ± 0.217 QH	78	78	32	32
10	12	57.29 ± 0.3222 ± 0.048 QH	57.29 ± 0.3222 ± 0.048 QH	36	36	32	32
11	13	57.29 ± 0.3222 ± 0.022 QH	57.29 ± 0.3222 ± 0.022 QH	16	16	32	32
12	14	57.29 ± 0.3222 ± 0.010 QH	57.29 ± 0.3222 ± 0.010 QH	8	8	32	32
13	15	57.29 ± 0.3222 ± 0.0045 QH	57.29 ± 0.3222 ± 0.0045 QH	3	3	32	32

Table 3. MWRI and GMI channel numbers, central frequency and polarization, bandwidth, and instantaneous field of view (IFOV).

Channel number		Central frequency (GHz) & polarization		Bandwidth (MHz)		IFOV(km)	
MWRI	GMI	MWRI	GMI	MWRI	GMI	MWRI	GMI
1	1	10.65 V	10.65 V	180	96.5	51 × 85	19 × 32
2	2	10.65 H	10.65 H	180	94.7	51 × 85	19 × 32
3	3	18.7 V	18.7 V	200	193	30 × 50	11 × 18
4	4	18.7 H	18.7 H	200	194	30 × 50	11 × 18
5	5	23.8 V	23.8 V	400	367	27 × 45	10 × 16
6	–	23.8 H	–	400	–	27 × 45	–
7	6	36.5 V	36.5 V	400	697	18 × 30	9 × 15
8	7	36.5 H	36.5 H	400	707	18 × 30	9 × 15
9	8	89.0 V	89.0 V	3000	5470	9 × 15	4 × 7
10	9	89.0 H	89.0 H	3000	5516	9 × 15	4 × 7

Notes: V, vertical; H, horizontal.

MWTS-2 spot. For MWRI, it was observed that the instrument on FY-3D has 266 fields of view (FOVs) (compared to 254 on FY-3C), and it was decided to discard the first and last six FOVs and proceed with the existing thinning already in place for FY-3C that takes every second spot across the track. This aims to avoid over sampling

To collocate observations and model fields, and quality control the data, FY-3D data have been processed in a clear-sky passive offline mode of the Met Office Observation Processing System (OPS). In operations, OPS runs an N1280L70 resolution (about a 10-km grid length in midlatitudes and 70 levels with the model top at 80 km) one-dimensional variational analysis (1D-Var). 1D-Var is used for quality control, to thin the observations, and to derive physical parameters for the subsequent main 4D variational assimilation. The background used for the comparison and the 1D-Var retrieval is the short-range forecast from the previous assimilation cycle, interpolated at the observation location and time. The fast radiative transfer model RTTOV version 12 (Saunders et al., 2018) is used to map model variables in the observation spectral domain. Surface emissivity is calculated using FASTEM 6 (Kazumori and English, 2015) over oceans and a fixed value is used over land (https://www.nwpsaf.eu/site/software/rttov/download/#Emissivity_BRDF_atlas_data; last accessed 6 March 2020). The main assimilation system is a hybrid 4-dimensional variational analysis (4D-Var) with a six-hour time window and background error information provided by a global ensemble (Lorenc et al., 2000; Rawlins et al., 2007).

Because FY-3D data are used passively (i.e., they are not assimilated in 4D-Var), the background used for the comparison is therefore independent from the observations. On the contrary, ATMS, FY-3C MWHS-2 and GMI are actively assimilated into the system, resulting in analyses and subsequent forecasts constrained by the value of their observations (depending on the weight given to the observations errors). Consequently, the difference between observations and the model background should be slightly lower for the assimilated instruments than the difference between observations from FY-3D and the model background.

In addition to background departure analyses (i.e., the observation-minus-background difference; hereafter, O-B), we investigate the double difference with instruments of equivalent radiometric capability. FY-3D MWTS-2 and MWHS-2 are compared to NOAA-20 ATMS equivalent channels and FY-3C MWHS-2 (FY-3C MWTS-2 data are not available over the period of study). FY-3D MWRI is compared to GPM GMI equivalent channels and FY-3C MWRI.

For this assessment, data are analyzed before bias correction. OPS standard quality controls are applied to all observations and consist of a gross error check on the observation location and the background, a convergence check, a radiative transfer error check, and a check on retrieved brightness temperature. Note that in operation, checks on observation brightness temperature and background departure are also conducted but are excluded from this analysis in order to evaluate

the entire range of observations (and not only the "good ones").

Two cloud tests are applied to MWTS-2 and MWHS-2. First, a maximum likelihood method, described by English et al. (1999), combines the first iteration of the 1D-Var based on observations at 183 ± 7, 183 ± 3 and 183 ± 1 GHz and an imposed threshold on the magnitude of the background departure at 183 ± 7 GHz. Second, a scattering test is based on the difference in brightness temperature at 89 and 150 GHz, and an index calculated as a function of the satellite zenith angle as described by Bennartz et al. (2002). For MWRI, a threshold imposed on the liquid water path retrieved in 1D-Var is set to 10 g m^{-2} and all observations with O-B greater than 4.3 K at 36.6 GHz (H) are marked as cloudy. Additionally, strongly scattering scenes are flagged and removed based on the anomaly (departure from the mean O-B) difference between 37 and 89 GHz.

ATMS benefits from the same cloud tests as the block MWTS-2 + MWHS-2. GMI benefits from the same tests as MWRI but also has an additional quality control based on the quality flag provided by NASA (this includes, for example, observations contaminated by radio frequency interference).

The observations used in this assessment are considered over ocean only, between 15 June and 15 September 2019. The results are discussed below.

3.1. *MWTS-2*

Figure 1a shows the mean O-B and standard deviation of O-B calculated for FY-3D MWTS-2 and ATMS at equivalent channel frequencies. The MWTS-2 mean bias ranges from −1.32 to 0.6 K. It is worth noting that those values are up to an order of magnitude smaller than the mean bias found for the instrument on FY-3C as evaluated by Lu et al. (2015). The FY-3D MWTS-2 and ATMS instruments have a consistent bias both in sign and magnitude across most channels, with an average difference of 0.36 ± 0.28 K (1σ), except at 54.40 GHz (channel 5) where the MWTS-2 bias reaches −1.32 K compared to −0.30 K for ATMS. The FY-3D MWTS-2 standard deviation of O-B varies from 2.9 to 0.36 K and is larger than the ATMS standard deviation by 0.36 K on average. For both instruments the standard deviation is large at frequencies sensitive to the surface and upper stratosphere, and low in the mid-troposphere and lower stratosphere.

The large standard deviation in the low-peaking and upper-stratospheric channels (channels 1–3 and 11–13, respectively) mostly results from a combination of model-driven biases that affect both instruments in a similar way. For surface-sensitive channels, the sea surface emissivity model used in the forward model for microwave frequencies, FASTEM, is known to suffer from systematic errors at low skin temperature (less than 275 K) and strong surface wind [see, for example, Carminati et al. (2017)]. The period of study spans austral winter (June–September), when low temperatures and strong winds become more frequent in the Southern Ocean, and where large positive biases have been
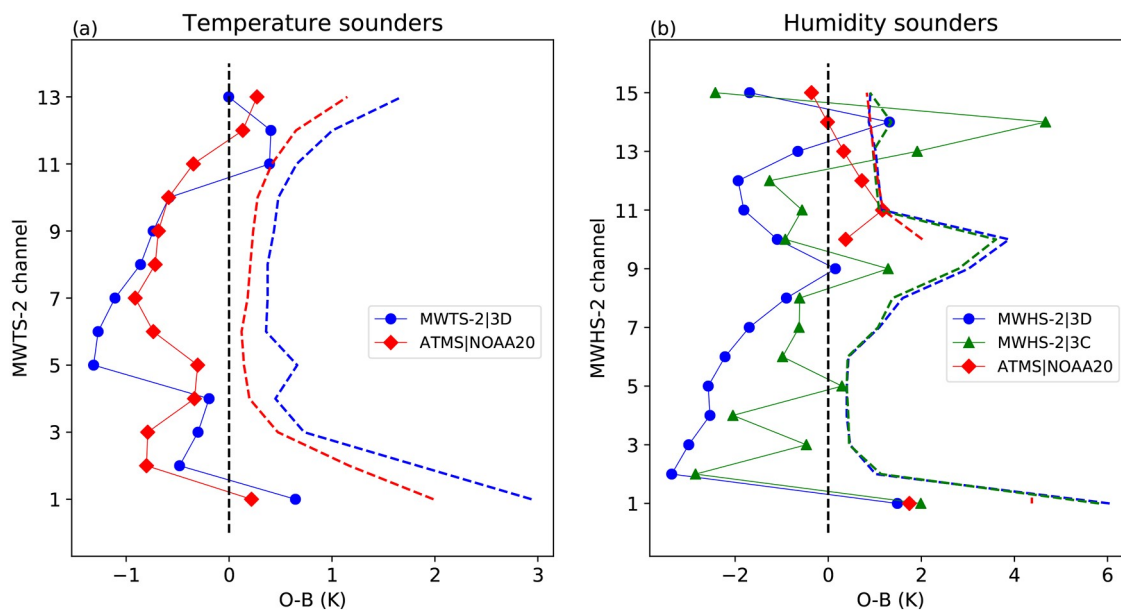
Fig. 1. (a) Mean background departure (O−B) and standard deviation of O−B for FY-3D MWTS-2 (blue) and NOAA-20 ATMS (red) low-scattering oceanic scenes averaged between 15 June and 15 September 2019. Solid lines show the mean and dashed lines the standard deviation. (b) As in (a) but for FY-3D MWHS-2 (blue), FY-3C MWHS-2 (green), and NOAA-20 ATMS (red).

detected in MWTS-2 and ATMS background departures (not shown) for these channels. Additionally, contamination from undetected residual cloud is more likely to affect these low-peaking channels and further increase the standard deviation. The increase in the standard deviation in the upper-stratospheric channels can be traced to geographically localized biases in the NWP model. These biases have been attributed to deficiencies in the parameterization of gravity waves breaking down in the stratosphere (private communication with Ed Pavelin, Met Office).

Channel 5, on the other hand, shows a clear distinction between MWTS-2 and ATMS, both in term of bias and standard deviation, suggesting an instrument-related problem. This channel is affected by a large 1.96-K edge-to-edge scan bias. Bias variations along the scan line greater than 1 K, associated in some instances with complex patterns, are visible in channels 1–6 and 13, and to a lesser extent in channels 7–12, as shown in Fig. 2a. Note that in Fig. 3, scan positions range from 1 to 30 because of the pre-processing step that averages one in three scan positions. Scan-dependent biases have been previously reported for the MWTS-2 instrument onboard FY-3C (Lu et al., 2015; Li et al., 2016; Tian et al., 2018). As suggested by Lu et al. (2015), a contamination of the antenna by the cold target could lead to lower-than-normal observed Earth temperature and subsequent cold bias in the O−B. This hypothesis is consistent with the negative O−B strengthening from scan position 1 to 22 observed in channels 1–8 in Fig. 2. For some channels, the bias stabilizes over the last six scan positions, possibly due to the antenna pattern correction. Although the root of the problem will have to be addressed through a revised antenna correction in the calibration system, bias corrections in place at the Met Office, ECMWF, or CMA have

been shown to efficiently remove the most detrimental effects (Lu et al., 2015; Li et al., 2016).

In their assessment of FY-3C MWTS-2, Lu et al. (2015) also highlighted a dependence of the bias on scene temperature. This happens when the observed temperature deviates from the linear assumption used for the interpolation of digital counts from cold to warm targets. This effect is generally removed by applying a nonlinearity correction in the calibration. In some instances, however, the correction is not optimized, as shown by Atkinson et al. (2015) for FY-3C MWTS-2. In order to investigate if such a dependency can be found in the FY-3D MWTS-2 dataset, we analyzed the O−B as a function of the background scene temperature calculating the slope and correlation of a linear least-squares regression along with those of ATMS for comparison. The results are reported in Table 4. Note that surface-sensitive channels are omitted from this analysis in order to avoid model-driven biases related to surface emissivity being entangled with instrument biases. MWTS-2 channels 5 (54.40 GHz), 13 (57.29 ± 0.322 ± 0.0045 GHz), and 6 (54.94 GHz) are the channels that present the largest background departure gradients (−0.047, −0.032 and −0.026 K K^{-1}, respectively). These are of the same order as reported by Lu et al. (2015) for FY-3C MWTS-2 and compare well with ATMS, although ATMS low-peaking channels tend to be less impacted than the high-peaking ones.

Additionally, Lu et al. (2015) detected a land–sea contrast in some FY-3C MWTS-2 upper-atmosphere channels. The problem was suspected to be caused by inter-channel interferences, but this has not been seen in the FY-3D dataset.

Biases along the satellite orbit [as described by Booton et al. (2014)] are also investigated. Figure 3a shows the back-
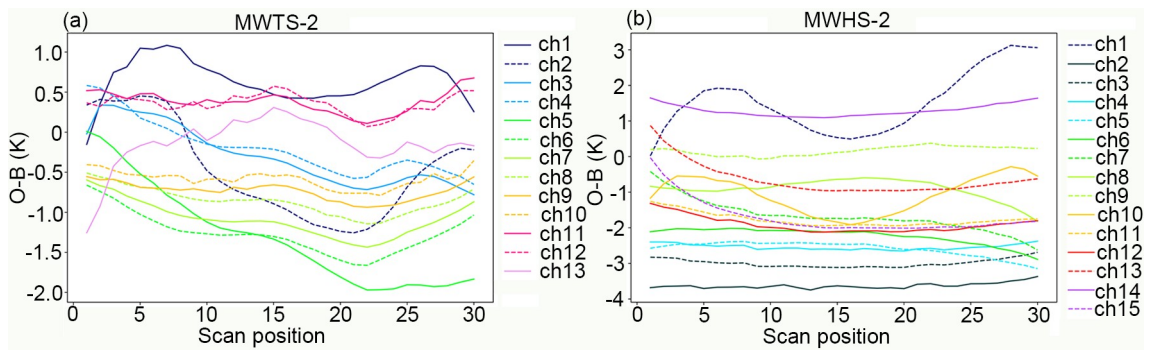
Fig. 2. (a) FY-3D MWTS-2 mean background departure as a function of the scan position for low-scattering oceanic scenes averaged over August 2019. (b) As in (a) but for FY-3D MWHS-2.
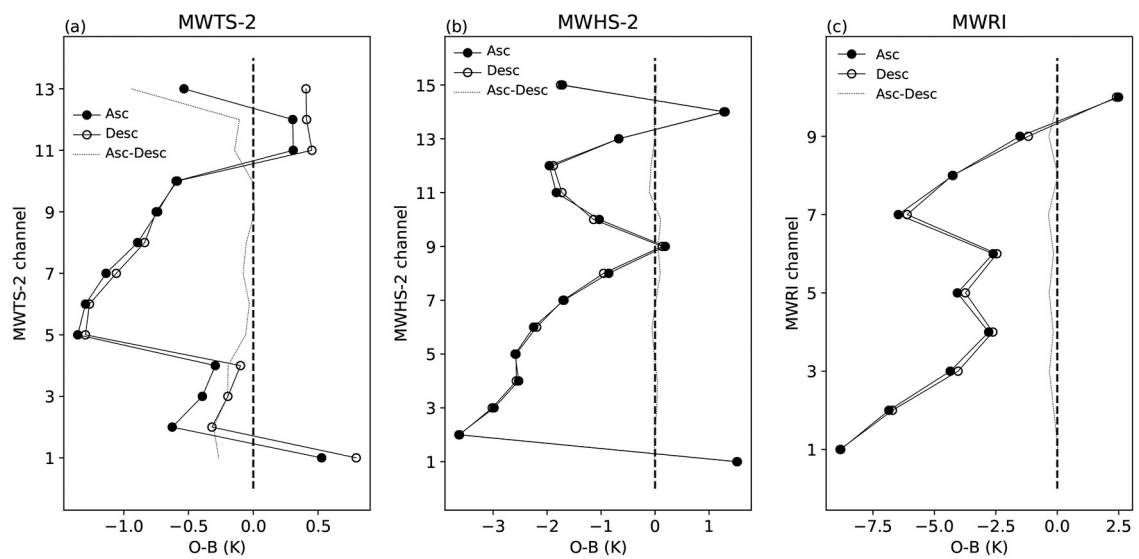
Fig. 3. (a) FY-3D MWTS-2 mean background departure from the ascending node (filled circles) and descending node (open circles) for low-scattering oceanic scenes averaged over August 2019. The gray line shows the difference, i.e., O-B ascending minus O-B descending. (b) As in (a) but for FY-3D MWHS-2. (c) As in (a) but for FY-3D MWRI.

Table 4. Slope, intercept, and correlation coefficient from a linear least-squares regression between the background scene temperature and FY-3D MWTS-2 O-B for low-scattering oceanic scenes in August 2019. The statistics are also shown for NOAA-20 ATMS.

	Slope (K K⁻¹)		Intercept (K)		r-value	
Frequency (GHz)	MWTS-2¦3D	ATMS	MWTS-2¦3D	ATMS	MWTS-2¦3D	ATMS
54.40	−0.047	0.003	9.73	−1.08	−0.40	0.12
54.94	−0.026	0.000	4.59	−0.64	−0.34	−0.02
55.50	0.001	0.011	−1.30	−3.32	0.01	0.31
57.29	0.006	0.009	−2.05	−2.59	0.12	0.32
57.29 ± 0.217	0.012	0.009	−3.56	−2.64	0.20	0.26
57.29 ± 0.322 ± 0.048	0.001	−0.002	−0.72	−0.17	0.01	−0.05
57.29 ± 0.322 ± 0.022	−0.014	−0.016	3.54	3.26	−0.15	−0.26
57.29 ± 0.322 ± 0.01	−0.017	−0.024	4.51	5.94	−0.12	−0.27
57.29 ± 0.322 ± 0.0045	−0.032	−0.040	7.81	10.08	−0.14	−0.27

ground departures from the ascending node, when the satellite sees the daytime side of Earth, compared to those of the nighttime descending node. O-B values in the descending node are lower than in the ascending node. This difference is larger than 0.1 K in the low (1–4) and high (11–13) peak-

ing channels and largest for channels 13 where the difference reaches −0.9 K. This bias is likely related to a calibration issue, discussed further below.

A cross-track disturbance, known as striping noise, has been detected and contributes to the instrument noise. Strip-

ing, also identified in ATMS temperature sounding channels, is a consequence of gain fluctuations in the instrument amplifier (Bormann et al., 2013). Li et al. (2016) and Lu et al. (2015) noted striping in the FY-3C MWTS-2 dataset. Li et al. (2016) calculated that FY-3C MWTS-2 striping affects all channels and ranges from 0.1 to 0.7 K in terms of standard deviation, noting that the striping patterns are not visible when the standard deviation of O-B is significantly larger. Here, we characterize this striping noise with the same index as presented by Lu et al. (2015); that is, the ratio of along-track to cross-track variability. The index, shown in Table 5, varies from 1.5 to 3.2, which is larger than for ATMS (1.0 to 1.6 in the temperature-sounding channels), but reduced compared to MWTS-2 on FY-3C.

The FY-3D MWTS-2 noise equivalent differential temperature (NEDT) is shown in Table 5. It is computed from the warm calibration counts as the standard deviation of the difference between warm counts and a rolling average over seven lines but excluding the line under test. The standard deviation of the counts differences is then normalized by the channel gain. The FY-3D MWTS-2 NEDT is similar or smaller to that reported by Lu et al. (2015) for FY-3C MWTS-2. It is also smaller than for ATMS, noting, however, that the onboard processing is different and the time interval between scans (and hence the integration time) is longer for MWTS-2. Note that there are significant correlations between FY-3D MWTS-2 adjacent samples in the calibration views, presumably due to the characteristics of the electronic filtering.

Investigating the source of the ascending—descending bias detected in FY-3D MWTS-2, we have used the instrument raw digital counts (i.e., level 0) from the onboard computer files to derive the antenna temperature and compare it to the reported temperature. As a first step, we averaged the raw counts across scan lines using a triangular function with a width of seven scan lines and compared it with that of CMA. As shown on Fig. 4, our averaging (blue) follows the raw data (black), while the CMA averaging (red) is shifted by a few scan lines. Such a displacement is consistent with the algorithm originally used on FY-3C that replaces all points outside one standard deviation away from the mean with the mean value of the 20 following samples. It was then argued that the averaging should instead use three standard deviations as the threshold to filter outliers and the outliers be replaced by a mean centered on its position (instead

of being based on the following points). A correction was later prepared for FY-3C but was not implemented in operations due to the failure of the instrument. Our results suggest that the FY-3D algorithm is similar to the original pre-correction algorithm used on FY-3C.

Using the Met Office averaged raw counts, we derived the antenna temperature with a linear calibration as in Atkinson et al. (2015) and compared it to the CMA antenna temperature as shown in Fig. 5. The difference between the Met Office and CMA antenna temperature reveals that the current algorithm used by the CMA causes the temperature to be up to 2 K warmer than that of the Met Office on the ascending node, and conversely 2 K colder on the descending node, explaining the observed ascending—descending bias. Note that this mainly affects channels 12 and 13. The impact is minor for lower-frequency channels. The cross-scan bias patterns visible in Fig. 5 also suggest a significant effect on the striping noise. It is therefore recommended that the CMA modifies the scheme used in the FY-3D MWTS-2 calibration system to correct for a shift of average raw counts causing the biases in the derived antenna temperature and ultimately systematic errors in level 1 brightness temperature. The issue is currently being investigated at the CMA (Dawei An, CMA, private communication, 2020).

3.2. MWHS-2

The global mean O-B over ocean has been calculated for FY-3D and FY-3C MWHS-2, and ATMS at equivalent channel frequencies (Fig. 1a). Background departures for FY-3D MWHS-2 are of similar magnitude but generally lower (except channel 15) than FY-3C. In the 183-GHz channels, FY-3D MWHS-2 O-B are found within ±1.9 K compared to ±4.5 K for the instrument on FY-3C, and ±1.2 K for ATMS. The ATMS bias at 183.31 ± 3 and ±4.5 GHz (MWHS-2 channel 13 and 14, respectively) does not exhibit a peak like the MWHS-2 instruments. This difference was also noted by Lawrence et al. (2018), who compared FY-3C MWHS-2 to ATMS and the Microwave Humidity Sounder onboard various U.S. and European platforms. The authors pointed out that while the biases at 183 GHz are consistent amongst most microwave instruments and could be related to biases in the radiative transfer modeling of this humidity band (Brogniez et al., 2016; Calbet et al., 2018), the different pattern observed for FY-3C MWHS-2 is more likely to be an instrument-related bias. The hypothesis of instrument-

Table 5. FY-3D MWTS-2 and MWHS-2 striping index and NEDT estimated from the warm calibration counts of the onboard computer files. The striping is calculated as the root-mean-square of the ratio of the along-track standard deviation to the cross-track standard deviation of the calibration view samples grouped into boxes of four pixels by four scans.

		Channel														
		1	2	3	4	5	6	7	8	9	10	11	12	13	14	15
MWTS-2	Striping index	3.2	2.4	2.7	2.0	1.9	2.3	1.9	1.7	1.8	1.6	1.6	1.8	1.5	−	−
	NEDT (K)	0.3	0.2	0.2	0.23	0.2	0.2	0.3	0.4	0.5	0.5	0.7	1.2	1.5	−	−
MWHS-2	Striping index	1.4	1.1	1.1	1.1	1.3	1.2	1.1	1.2	1.3	1.2	1.2	1.4	1.5	1.2	1.5
	NEDT (K)	0.3	2.5	1.0	0.8	0.8	0.7	0.7	0.3	0.3	0.4	0.6	0.5	0.4	0.4	0.4
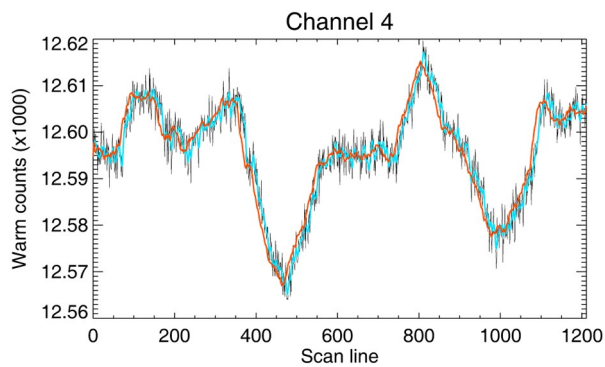
Fig. 4. Average warm calibration counts of MWTS-2 FY-3D channel 4. Raw data are shown in black, CMA averaging in red, and Met Office averaging in blue.

related bias is further supported by the similar bias found on FY-3D MWHS-2, which has the same design and characteristics as its predecessor. The shift in O-B between the two MWHS-2 instruments could be due to their different pre-launch calibration setup, including the correction of biases from the warm and cold targets, the derivation of coefficients for the nonlinearity correction, and the correction for channels breaking the monochromatic assumption, which have been derived using a new thermal vacuum test facility as described by Wang et al. (2019). The authors found that FY-3D MWHS-2 channel 14 is affected by a radiation leakage originating from the receiver used for the high-frequency channels (150 and 183 GHz). The antenna-leaked radiation bounced back from the device surroundings unless covered with a black body absorber. They concluded that this should not impact operational performances since there are no such surroundings in space. However, both Lawrence et al. (2017, 2018) and Carminati et al. (2018) noted that FY-3C MWHS-2 channels 13 and 14 have been experiencing large bias shifts and drifts that are strongly correlated with the temperature of the instrument's environment. The implications of this are that the susceptibility of those channels sensitive to temperature changes may be related to the leakage highlighted by Wang et al. (2019) through contamination by the radiation directly emitted by the platform, or by the antenna's emission interacting with the body of the plat-

form, or a combination of both.

In the 118-GHz channels, the findings are similar. The FY-3D MWHS-2 bias decreases relatively smoothly, from high- to low-peaking channels, to become positive in the lowermost surface-sensitive channel (channel 9). Although this reduction of bias with the decrease in the height of sensitivity is also visible for FY-3C MWHS-2, the channel-to-channel variation is more erratic.

The standard deviation of O-B for FY-3D MWHS-2 varies from 0.4 to 1.6 K (ignoring window channels 1, 9 and 10). It is comparable to that of FY-3C at most channels and significantly smaller (0.48 K smaller) at channel 14. It is also comparable to that of ATMS at 183 GHz but larger in the window channels (noting that the frequency is not exactly the same between the two instruments). Apart from the window channels, the standard deviation in this analysis is smaller than that reported by Guo et al. (2019).

The variation of O-B with the scan position is also analyzed for FY-3D MWHS-2 (Fig. 2a). Window channels 1 and 10 (89 and 150 GHz, respectively) present the distinctive double maxima towards the edge of the scan with up to 3.1 K peak-to-peak amplitude, somewhat similar in shape to those of MWTS-2 window channel 1 and 2 (50.3 and 51.76 GHz, respectively). Interestingly, the 118-GHz surface-sensitive channels (channels 8 and 9) do not present such a pattern, which seems to only affect channels with a quasi-horizontal polarization. Channels 11, 12, 13 and 15 have a maximum on the left edge of the scan (position 1); channels 5, 6 and 8 have a minimum on the right edge (position 30); and channel 7 has both features with an edge-to-edge difference of 2.2 K.

Li et al. (2016) also analyzed FY-3C MWHS-2 striping noise and showed that it affects all channels with a standard deviation of up to 0.8 K. Our estimation of the striping index ranges from 1.1 to 1.5. The NEDT varies from 0.3 to 2.5 K. This is larger than that reported by Guo et al. (2019) for channels 2–7, and similar elsewhere. The striping index and the NEDT are summarized in Table 5.

Investigating the difference between ascending and descending nodes (Fig. 3b), we found that both nodes are very consistent with each other, with an average difference of
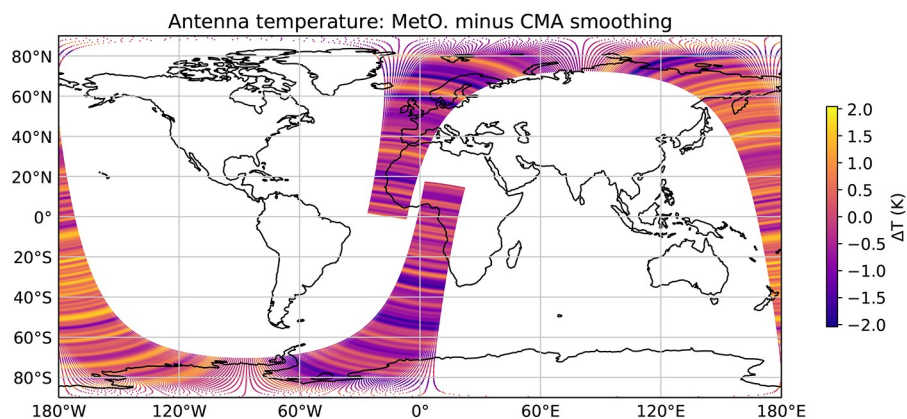
Fig. 5. FY-3D MWTS-2 Met Office-derived minus original antenna temperature (channel 13).

Table 6. As in Table 4 but for FY-3D MWHS-2, FY-3C MWHS-2, and ATMS.

| Frequency (GHz)	Slope (K K⁻¹)			Intercept (K)			r-value		
	MWHS-2⎮3D	MWHS-2⎮3C	ATMS	MWHS-2⎮3D	MWHS-2⎮3C	ATMS	MWHS-2⎮3D	MWHS-2⎮3C	ATMS
118.75 ± 0.08	0.029	0.037	–	−10.38	−11.18	–	0.20	0.22	–
118.75 ± 0.2	0.027	0.019	–	−8.85	−4.57	–	0.44	0.33	–
118.75 ± 0.3	0.026	0.031	–	−8.12	−8.74	–	0.50	0.56	–
118.75 ± 0.8	0.014	0.003	–	−5.71	−0.41	–	0.19	0.04	–
118.75 ± 1.1	0.021	0.031	–	−7.18	−8.44	–	0.32	0.47	–
183 ± 1.0	0.027	0.014	0.014	−8.56	−4.09	−2.28	0.19	0.10	0.10
183 ± 1.8	0.014	0.012	0.005	−5.58	−4.42	−0.44	0.11	0.10	0.03
183 ± 3.0	−0.017	0.014	−0.001	3.72	−1.76	0.51	−0.13	0.11	−0.01
183 ± 4.5	−0.017	0.062	0.005	5.72	−12.01	−1.30	−0.14	0.34	0.04
183 ± 7.0	−0.010	0.037	0.014	1.11	−12.48	−4.31	−0.08	0.29	0.13

0.01 K.

Linear regressions of the O-B as a function of the scene temperature were calculated for FY-3D MWHS-2 channels 2–6 and 11–15, and the slopes, intercepts and correlation coefficients are shown in Table 6 along with those of FY-3C MWHS-2 and ATMS (at equivalent frequencies). Background departure gradients are similar between the two MWHS-2 instruments in the 118-GHz channels. The most sensitive channel to scene temperature is 118.75 ± 0.08 GHz, with slopes of 0.029 and 0.037 K K⁻¹ (correlation of 0.20 and 0.22) for FY-3D and FY-3C MWHS-2, respectively. Interestingly, those results are of the same order as for the temperature channels sounding the 54–57-GHz oxygen band on MWTS-2 (see Table 4). In the 183-GHz channels, O-B gradients for the ATMS and MWHS-2 instruments are similar. We note a significant reduction of the scene temperature dependence at 183 ± 4.5 GHz from FY-3C to FY-3D, with the gradient decreasing from 0.062 to −0.017 K K⁻¹ and the correlation from 0.34 to −0.14.

3.3. MWRI

The MWRI instrument onboard FY-3C has been thoroughly evaluated by Lawrence et al. (2017). Here, we evaluate the instrument onboard FY-3D in the light of their findings and in comparison to FY-3C MWRI and GMI. Figure 6 shows the mean O-B and standard deviation of O-B for all three instruments. Global biases are consistent in shape between the two MWRI instruments, although reduced on FY-3D by more than 1 K compared to FY-3C in channels 1–4, 7 and 10, and to a lesser extent in channels 5 and 6. The bias has increased in channels 8 and 9 by 1.6 and 0.3 K, respectively. Compared to GMI, FY-3D MWRI remains cold-biased (from 10.6 K at 10 GHz to 1.2 K at 89 GHz), as previously noted by Lawrence et al. (2017) for the instrument on FY-3C.

The FY-3D MWRI standard deviation of O-B is reduced by 0.1 to 0.6 K compared to the instrument on FY-3C, except for channel 7, for which it is 3.4 K larger. The larger standard deviation in channel 7 is further discussed below. This reduction in standard deviation is consistent with the correction applied by the CMA (only to FY-3D
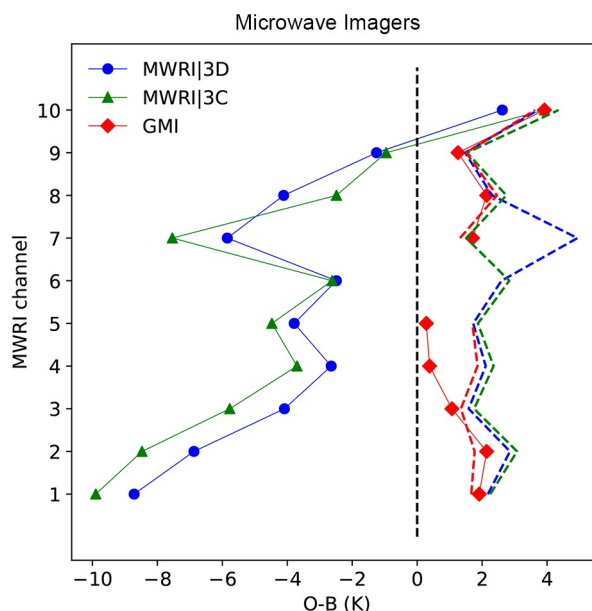
Fig. 6. Mean background departure (solid lines) and standard deviation of O-B (dashed lines) for FY FY-3D MWRI (blue), FY-3C MWRI (green), and GPM GMI (red) low-scattering oceanic scenes averaged between 15 June and 15 September 2019.

MWRI to the best of our knowledge) to the warm target that used to suffer from a contamination of the warm load view from the Earth scene affecting the warm reflector back lobe. This correction has been presented by Shengli WU (National Satellite Meteorological Center of the CMA) at the Global Space-based Inter-Calibration System (GSICS) meeting in Shanghai 2018 (http://gsics.atmos.umd.edu/bin/view/Development/20180319; presentation 9b; last accessed 6 March 20). The standard deviation also compares well to that of GMI at 18, 23, 36 and 89 GHz. The larger difference observed at low frequency can be explained by the larger field of view of MWRI compared to GMI (see Table 3), which is eventually contaminated by land surface in coastal areas.

Investigating the peak in background departure (and

FY-3D MWRI 36.5GHz (V) 2019-07-25
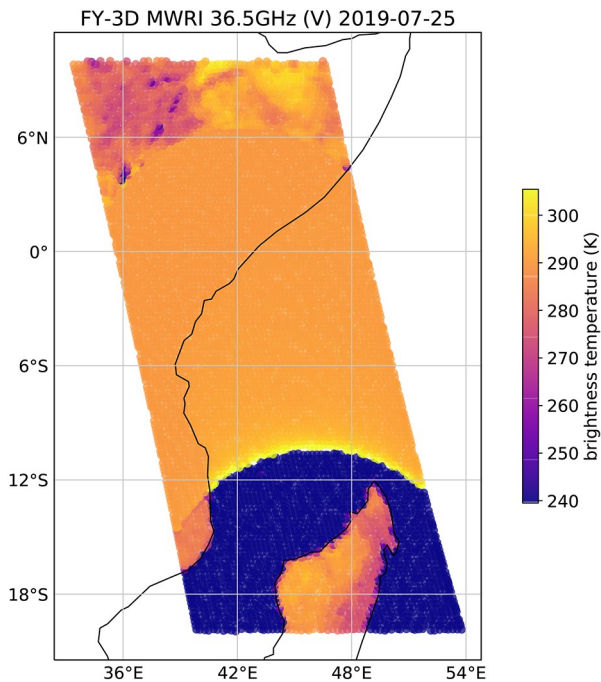
Fig. 7. FY-3D MWRI unscreened observations at 36.5 GHz V-pol (channel 7) shown north of Madagascar on 25 July 2019.

standard deviation) affecting channel 7, we have noted anomalies in the observations affecting small sections of the instrument swath between 13 July and 10 August 2019. Figure 7 illustrates an example of anomalously large brightness temperature affecting the MWRI swath north of Madagascar on 25 July 2019. Around 12°S, the observed brightness temperature suddenly shifts from ~220 K (over ocean) to more than 280 K, regardless of the surface (land or ocean) across all scan lines before returning to normal at around 6°N. This event was not flagged in MWRI raw data distributed by the CMA (i.e., neither in QA_Ch_Flag nor QA_Scan_Flag). The origin of the problem remains unexplained to date.

The foremost issue with FY-3C MWRI, as highlighted by Lawrence et al. (2017), is a strong solar-dependent bias leading to differences between the ascending and descending nodes as large as 2 K and consistent across all channels. Such a bias, previously detected in legacy imagers (Bell et al., 2008; Geer et al., 2010), results from thermal emissions from sun-heated element(s) of the instrument (usually the main antenna) contaminating the received signal and unaccounted for in the calibration. The three-point calibration of MWRI, however, compensates for any contamination from the main receiver, leading Lawrence et al. (2017) to suggest that the reflectors dedicated to the warm and cold targets (whose emissions are unaccounted for in the calibration) may contribute significantly to the ascending—descending bias. Because such a bias is complex to understand and all the more difficult to correct in the context of NWP systems, MWRI observations have not been used in data assimilation systems, except at the CMA and the Met Office (see next section).

For FY-3D MWRI, Xie et al. (2018) developed a phys-

ical-based bias correction linking the observed brightness temperature to the temperature of the hot load reflector. According to the authors, the post-correction ascending/descending bias is reduced to less than 0.2 K. Figure 3c shows consistent results, with an ascending-minus-descending bias varying from −0.36 to 0.08 K (−0.17 K on average).

The successful removal of the solar-dependent bias of MWRI on FY-3D will have a significant impact for the future use of the instrument in NWP centers because they will be able to assimilate its observations without having to implement complex bias corrections. It must be noted, however, that another feature highlighted by Lawrence et al. (2017) was the drift in time of the FY-3C MWRI global bias (up to 2 K in four years) in parallel with the increase in amplitude of the solar-dependent bias, the latter potentially the cause of the former. Because the reflector emissivity correction applied by the CMA is a one-time change, it will be important to closely monitor the bias of MWRI over time and apply an updated correction if a degradation is detected.

Finally, we note that both Zou at al. (2012) and Lawrence et al. (2017) reported radio frequency interferences (RFIs) affecting MWRI onboard FY-3B and FY-3C. Shengli WU (CMA) has communicated (https://digitalcommons.usu.edu/calcon/CALCON2019/all2019content/7/; last accessed 6 March 2020) that, for FY-3D MWRI, RFI affects both the 10- and 18-GHz channels and that the CMA is working on a correction algorithm.

4. Assimilation in the Met Office NWP system

Assimilation experiments have been conducted over the period 15 June to 15 September 2019. The baseline is a low resolution (N320L70 forecast, N108/N216 4D-Var uncoupled hybrid) full global system similar to that used in operation at the Met Office since 4 December 2019. The radiances assimilated in the global system are from AQUA AIRS, F-17 SSMIS, FY-3B MWHS-1, FY-3C MWRI, FY-3C MWHS-2, GCOMW AMSR-2, GOES 15 Imager, GOES 16 ABI, GPM GMI, HIMAWARI 8 AHI, MT SAPHIR, SNPP ATMS, SNPP CrIS, MetOp B ATOVS, MetOp B IASI, MetOp A ATOVS, MetOp A IASI, MSG 1 SEVIRI, MSG 4 SEVIRI, NOAA-15 ATOVS, NOAA-18 ATOVS, NOAA-19 ATOVS, NOAA-20 ATMS, and NOAA-20 CrIS (acronyms are defined in the Appendix).

The experiments are:
- baseline only (Control);
- FY-3D MWHS-2 channels 11–15 assimilated on top of the Control (EXP 1);
- same as EXP 1 plus the addition of FY-3D MWTS-2 channels 4–13 (EXP 2);
- same as EXP1 plus the addition of FY-3D MWTS-2 high-peaking channels 9–13 only (EXP 3);
- FY-3D MWRI channels 3–8 assimilated on top of the Control with both FY-3C and FY-3D MWRI thinned to 120 km (EXP 4).

For these experiments, MWHS-2 channels 11–14 are rejected over sea ice and high land (orography > 1000 m), and channel 15 rejected over sea ice and land. MWTS-2 channels 4 is rejected over sea ice and land, channel 5 rejected over tropical land, and channels 5–7 over high land. MWHS-2 and MWTS-2 observations are thinned every 154 km in the tropics and 125 km in the extratropics. MWRI channels are rejected over sea ice and land and the observations are thinned every 120 km (80 km in the control). Observation errors used in 4D-Var replicate those derived for FY-3C. The variational bias correction applied to MWHS-2 and MWTS-2 uses seven predictors, including a constant bias offset, two atmospheric thickness predictors (200–50 hPa and 850–300 hPa), and four Legendre polynomial predictors correcting the scan biases after a static spot-dependent offset is applied. For MWRI, two more predictors are used to correct the orbital bias [the cosine and sine of the Fourier series; see Booton et al. (2014)]. Offline runs over the same period have been used to spin up the bias predictors, and the first five days of the experiments are excluded from the verification to allow the variational bias correction to adjust for the new instruments.

The impact on the forecasts from adding the new instruments is evaluated through the change in RMSE for selected atmospheric variables in a range of forecast lead times. The RMSE change is calculated against Met Office analyses as shown in Fig. 8, ECMWF analyses, and conventional observations. Additionally, we evaluate how the other instruments respond to the new data by calculating the ratio of standard deviation of O-B in the experiment and the control. An improved observation fit to the background (i.e., reduced standard deviation) is the sign that the new data are having a positive impact on the atmospheric variables in the short-range forecasts used as background for the assimilation of satellite radiances. Figure 9 shows the change in observation fit to the background for NOAA-20 ATMS in EXPs 1–3 and GPM GMI in EXP 4.

The addition of MWHS-2 alone (EXP 1) results in a 0.1% overall reduction of the forecast RMSE and, although we note some small degradation in the Southern Hemisphere (SH), there are clear signs of improvement in the Northern Hemisphere (NH) and the tropics for low-level wind and geopotential height, as well as temperature across most lead times. The fit to the background for independent sounders is mostly neutral (see, for example, ATMS in Fig. 9a).

The addition of MWTS-2 along with MWHS-2 (EXP 2) results in an overall neutral change in forecast RMSE (0.05%) but causes significant degradation at short lead times, mostly in the SH, and to a lesser extent in the tropics and NH. We also note a persistent negative signal in the tropical upper-tropospheric temperature. In addition, the background fit of microwave instruments with channels sensitive to tropospheric and lower-stratospheric temperature has significantly degraded, as can be seen for ATMS channels 6–11 (equivalent to MWTS-2 channels 4–9) in Fig. 9b. The largest degradation (about 1%) occurs for ATMS channels 8

and 9, which peak in the upper troposphere. On the contrary, the highest-peaking channels, 12–15, which are sensitive to upper-stratospheric temperature, are improved by more than 1%. The degradation of the background fit for channels peaking in the troposphere is unsurprising given that it is a well observed part of the atmosphere with small errors and low level of uncertainty in the background. The large striping (not corrected, unlike the scan bias for example) in MWTS-2 observations is therefore introducing more noise than useful information into the system. In the upper stratosphere, however, the lower number of available observations drives up the uncertainty in the background to the extent that MWTS-2 channels, albeit noisy, can still yield benefits. This observation has motivated the setup of EXP 3 where only MWTS-2 high-peaking channels have been retained for assimilation.

The overall benefits gained with EXP 3 are similar to EXP 1 (0.1% change in RMSE) but without the degradation previously observed in the SH. Improvements span all three latitudinal bands and all variables, although mostly limited to lead times ranging from T+0 to T+60. A clear improvement is also visible in the background fit of ATMS (Fig. 9c), which has lost the degradation seen in channels 6–11 in EXP 2 but retained the improvement gained in the high-peaking channels. ATMS humidity channels have a slightly degraded fit, but the overall impact remains positive.

The addition of MWRI radiances on top of the baseline has resulted in a neutral change in RMSE (0.08% larger than the control), although some persistent degradations are visible in the tropics, especially for low-level temperature, but noting that these degradations are not detected when compared against ECMWF analyses or observations (overall RMSE 0.05% larger and 0.01% smaller, respectively; not shown). This therefore points to a possible deficiency in the representation of the tropical temperature in the Met Office analyses. The new data also have a mostly neutral impact on the fit to the background for most sounders, but result in a small improvement, consistent across all channels, for GMI (up to 0.3%; Fig. 9d) as well as SSMIS (up to 1.3%; not shown). The fit for AMSR-2 has degraded slightly, by 0.2%–0.4% (not shown).

In summary, the assimilation of radiances from FY-3D microwave instruments have a neutral to positive impact on the system (as expected, this is similar to the impact obtained when FY-3C instruments were introduced into the system), with the best results obtained for the assimilation of MWHS-2 channels 11–15 along with MWTS-2 channels 9–13. Note that a combined assessment of MWHS-2, MWTS-2 and MWRI has not been tested to date. Pending further evaluation, including high-resolution experiments, the addition of FY-3D microwave radiances is a potential candidate for the next model upgrade planned for June 2020.

5. Conclusion

FY-3D is the latest Chinese satellite in Sun-synchron-
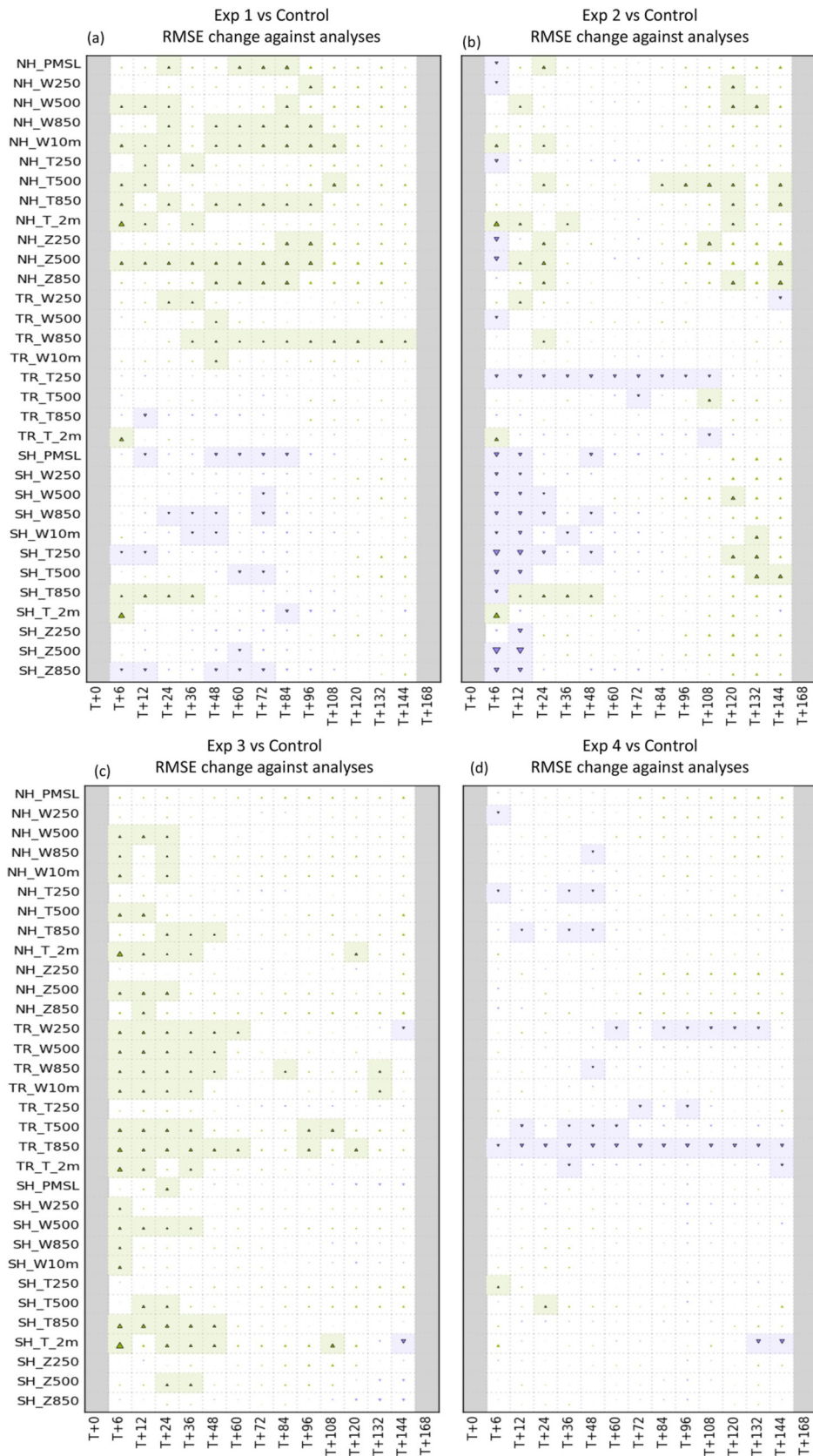
Fig. 8. Change in the root-mean-square forecast error between EXP (a) 1, (b) 2, (c) 3 and (d) 4 and the control for key atmospheric variables (see Appendix for acronyms) with respect to Met Office analyses over the period 15 June to 15 September 2019. The columns are the forecast time, out to six days. Upward-pointing green triangles denote improvement and downward-pointing purple triangles denote degradation. Shading shows significant changes.
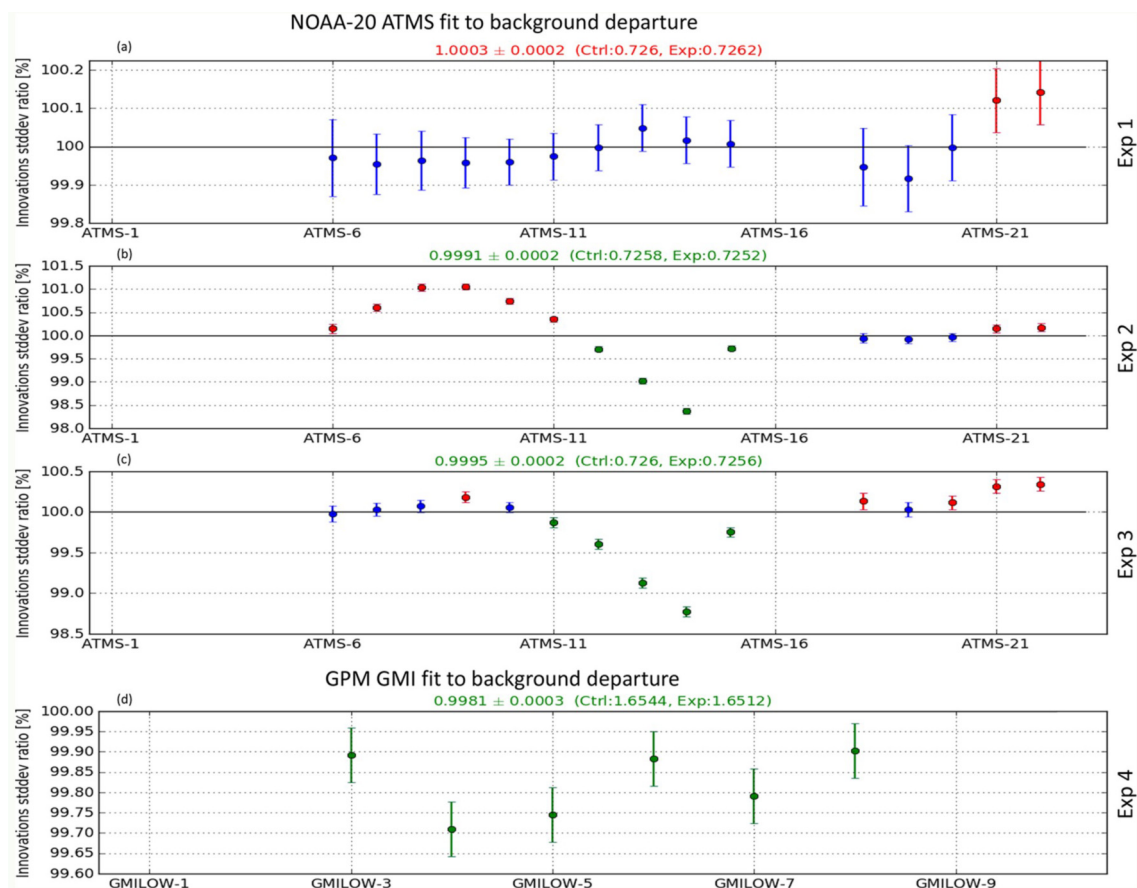
Fig. 9. Change in standard deviation of O-B for (a–c) NOAA-20 ATMS in EXP 1, 2 and 3, respectively, and (d) GMI in EXP 4, over the period 15 June 15 September 2019. Red indicates a significant increase, green a significant decrease, and blue no significant change. The numbers at the top of each plot indicate the mean change across all channels (±1σ).

ous orbit dedicated to weather and climate monitoring. In this study we have provided a characterization of the data quality for FY-3D microwave instruments, i.e., MWTS-2, MWHS-2 and MWRI, and evaluated their impact on the Met Office NWP system. FY-3D observations have been compared to the Met Office short-range forecasts, along with observations from the previous Chinese platform, FY-3C, carrying identical instruments (apart from MWTS-2, which is out of service), as well as observations from NOAA-20 ATMS and GPM GMI, two well-characterized U.S. instruments.

We first assessed MWTS-2 background departures and compared them to those of ATMS at equivalent channel frequencies. Because we could not compare FY-3D MWTS-2 with the FY-3C version, we analyzed our results in the light of previous assessment studies. The most interesting finding was a close agreement in global background departures with those from ATMS. This represents a significant improvement since the temperature sounder on FY-3C was shown to suffer a large cold inter-satellite bias attributed to a suboptimal calibration. The difference between FY-3D MWTS-2 and ATMS O-B is on average 0.36 ± 0.28 K (1σ). However, FY-3D MWTS-2 still suffers a strong scan-dependent bias that can reach amplitudes of up to 2 K and affects, to various extents, all channels. Striping noise and biases varying

with the scene temperature have also been detected in line with previous findings related to the instrument on FY-3C. We have also raised concerns regarding the smoothing method employed by the CMA to average the instrument's raw digital counts, which leads to an increase in striping noise and causes a bias of up to 0.9 K between the ascending and descending nodes. This method was also used for FY-3C MWTS-2 but was later revised by the CMA. We recommend that it should be revised for the instrument on FY-3D as well.

The assessment of FY-3D MWHS-2, in comparison to its predecessor on FY-3C and ATMS at equivalent channel frequencies, has revealed a shift in global bias, likely due to a different calibration with respect to the FY-3C version. This shift results in a reduction of the global bias in the 183-GHz humidity channels and places FY-3D MWHS-2 within ± 1.9 K to ATMS O-B. Like the instrument on FY-3C, the new MWHS-2 shows the signs of spurious sensitivity to the temperature of the instrument's environment in channel 14, and to a lesser extent channel 13, possibly linked to an emissivity leakage affecting the antenna. In the 118-GHz channels, the shift in global bias results in a lower but albeit more coherent channel-to-channel bias structure than FY-3C. The standard deviation of O-B is found to be similar or

smaller than that for FY-3C MWHS-2. Consistent with previous evaluations of FY-3C MWHS-2, we have detected the presence of striping noise.

From the evaluation of FY-3D MWRI, we have highlighted a reduction in the global biases across most channels, as well as a reduction in the standard deviation of O-B compared to the FY-3C version. The latter is consistent with the bias correction developed by the CMA aimed at reducing the noise in the warm target used for the calibration. Compared to GMI, the new MWRI remains low-biased but shows better agreement in terms of standard deviation. Focusing on the solar-dependent bias that was found to be as large as 2 K for the instrument on FY-3C and a serious drawback for use in NWP systems, we have shown that this bias has been reduced to 0.17 K on average for FY-3D MWRI. This is also the direct result of an improved correction applied by the CMA targeting the emissivity of the cold and hot reflectors. It is hoped that the CMA will also apply the emissivity correction to the instrument on FY-3C. Of particular concern, however, are the unrealistically large brightness temperatures recorded on several occasions between 13 July and 10 August 2019. This only affected channel 7 (36.5 GHz V-pol) and caused an inflation of the mean background departure and standard deviation in that channel. The cause of this problem is under investigation.

Assimilation experiments using a low-resolution version of the global Met Office NWP system have demonstrated the potential benefits of adding MWHS-2 and MWTS-2, on top of an already well-furnished observing system, a sign that saturation has not yet been reached in the microwave spectral domain. The best configuration, MWHS-2 channels 11–15 and MWTS-2 channels 9–13, provides a reduction in the forecast RMSE of 0.1% and improves the fit to the background for independent sounders by up to 1%. The addition of FY-3D MWRI has a mostly neutral impact on the forecast but improves the fit to the background of other imagers such as GMI or SSMIS (although not AMSR-2). All three instruments are candidates for the next model upgrade planned for mid-2020. Future work will focus on the assimilation of MWHS-2 118-GHz channels (along with 183 GHz) with an all-sky approach as it is currently done at the Met Office for other microwave humidity sounders.

In conclusion, this study has demonstrated an overall improvement of the data quality from FY-3D instruments with respect to their predecessors. The set of microwave instruments that FY-3D offers will further strengthen and increase the resiliency of the microwave branch of the observing system used for NWP, reduce forecast errors, and be more straightforward to use thanks to the mitigation of serious issues affecting past instruments.

APPENDIX

Assimilation experiments were verified against a series of atmospheric variables, listed below:

Northern Hemisphere Pressure at Mean Sea Level (NH_PMSL)

Northern Hemisphere Wind at 250 hPa (NH_W250)

Northern Hemisphere Wind at 500 hPa (NH_W500)

Northern Hemisphere Wind at 850 hPa (NH_W850)

Northern Hemisphere Wind at 10 m (NH_W10m)

Northern Hemisphere Temperature at 250 hPa (NH_T250)

Northern Hemisphere Temperature at 500 hPa (NH_T500)

Northern Hemisphere Temperature at 850 hPa (NH_T850)

Northern Hemisphere Temperature at 2 m (NH_T_2m)

Northern Hemisphere geopotential height at 250 hPa (NH_Z250)

Northern Hemisphere geopotential height at 500 hPa (NH_Z500)

Northern Hemisphere geopotential height at 850 hPa (NH_Z850)

Tropical Wind at 250 hPa (TR_W250)

Tropical Wind at 500 hPa (TR_W500)

Tropical Wind at 850 hPa (TR_W850)

Tropical Wind at 10 m (TR_W10m)

Tropical Temperature at 250 hPa (TR_T250)

Tropical Temperature at 500 hPa (TR_T250)

Tropical Temperature at 850 hPa (TR_T250)

Tropical Temperature at 10 m (TR_T250)

Southern Hemisphere Pressure at Mean Sea Level (NH_PMSL)

Southern Hemisphere Wind at 250 hPa (SH_W250)

Southern Hemisphere Wind at 500 hPa (SH_W500)

Southern Hemisphere Wind at 850 hPa (SH_W850)

Southern Hemisphere Wind at 10 m (SH_W10m)

Southern Hemisphere Temperature at 250 hPa (SH_T250)

Southern Hemisphere Temperature at 500 hPa (SH_T500)

Southern Hemisphere Temperature at 850 hPa (SH_T850)

Southern Hemisphere Temperature at 2 m (SH_T_2m)

Southern Hemisphere geopotential height at 250 hPa (SH_Z250)

Southern Hemisphere geopotential height at 500 hPa (SH_Z500)

Southern Hemisphere geopotential height at 850 hPa (SH_Z850)

List of instruments referenced in this paper

Earth Observation System Aqua Atmospheric Infra-Red Sounder (Aqua AIRS)

Defense Meteorological Satellite Program – F17 Special Sensor Microwave - Imager/Sounder (F-17 SSMIS)

Fengyun 3B Micro-Wave Humidity Sounder – 2 (FY-3B MWHS-1)

Fengyun 3C Micro-Wave Temperature Sounder – 2 (FY-3C MWTS-2)

Fengyun 3C Micro-Wave Humidity Sounder – 2 (FY-3C MWHS-2)

Fengyun 3C Micro-Wave Radiation Imager (FY-3C MWRI)

Global Change Observation Mission for Water Advanced Microwave Scanning Radiometer - 2 (GCOMW AMSR-2)

Geostationary Operational Environmental Satellite 15 Imager (GOES 15 Imager)

Geostationary Operational Environmental Satellite 16 Advanced Baseline Imager (GOES 16 ABI)

Global Precipitation Measurement Microwave Imager (GPM GMI)

Himawari 8 Advanced Himawari Imager (HIMAWARI 8 AHI)

Megha-Tropiques Sondeur Atmospherique du Profil d'Humidite Intertropicale par Radiometrie (MT SAPHIR)

Suomi National Polar-orbiting Partnership Advanced Technology Microwave Sounder (SNPP ATMS)

Suomi National Polar-orbiting Partnership Cross-track Infrared Sounder (SNPP CrIS)

Meteorological operational satellite – B Advanced TIROS Operational Vertical Sounder (MetOp-B ATOVS)

Meteorological operational satellite – B Infrared Atmospheric Sounding Interferometer (MetOp-B IASI)

Meteorological operational satellite – A Advanced TIROS Operational Vertical Sounder (MetOp-A ATOVS)

Meteorological operational satellite – B Infrared Atmospheric Sounding Interferometer (MetOp-A IASI)

Meteosat-8 Spinning Enhanced Visible Infra-Red Imager (MET-8 SEVIRI)

Meteosat-11 Spinning Enhanced Visible Infra-Red Imager (MET-11 SEVIRI)

National Oceanic and Atmospheric Administration – 15 Advanced TIROS Operational Vertical Sounder (NOAA-15 ATOVS)

National Oceanic and Atmospheric Administration – 18 Advanced TIROS Operational Vertical Sounder (NOAA-18 ATOVS)

National Oceanic and Atmospheric Administration – 19 Advanced TIROS Operational Vertical Sounder (NOAA-19 ATOVS)

National Oceanic and Atmospheric Administration – 20 Advanced Technology Microwave Sounder (NOAA-20 ATMS)

National Oceanic and Atmospheric Administration – 20 Cross-track Infrared Sounder (NOAA-20 CrIS)

REFERENCES

Atkinson, N., Q. F. Lu, B. Bell, F. Carminati, K. Lean, N. Bormann, and H. Lawrence, 2015: The FY-3C Evaluation Project: Microwave Sounder Calibration and Direct Broad-

cast Experiences. [Available from https://cimss.ssec.wisc.edu/itwg/itsc/itsc20/papers/1_02_atkinson_paper.pdf.]

Bauer, P., A. Thorpe, and G. Brunet, 2015: The quiet revolution of numerical weather prediction. *Nature*, **525**, 47–55, https://doi.org/10.1038/nature14956.

Bell, W., and Coauthors, 2008: The assimilation of SSMIS radiances in numerical weather prediction models. *IEEE Trans. Geosci. Remote Sens.*, **46**, 884–900, https://doi.org/10.1109/TGRS.2008.917335.

Bennartz, R., A. Thoss, A. Dybbroe, and D. B. Michelson, 2002: Precipitation analysis using the advanced microwave sounding unit in support of nowcasting applications. *Meteorological Applications*, **9**(2), 177–189, https://doi.org/10.1017/S1350482702002037.

Berg, W., and Coauthors, 2016: Intercalibration of the GPM microwave radiometer constellation. *J. Atmos. Oceanic Technol.*, **33**(12), 2639–2654, https://doi.org/10.1175/JTECH-D-16-0100.1.

Bobak, J. P., D. J. Dowgiallo, T. E. vonRentzell, and N. R. McGlothlin, 2005: Satellite calibration and validation utilizing the Airborne Polarimetric Microwave Imaging Radiometer (APMIR). Proc. OCEANS 2005 MTS/IEEE, Washington, DC, IEEE, 352–354, doi: 10.1109/OCEANS.2005.1639787.

Booton, A., W. Bell, and N. Atkinson, 2014: An improved bias correction for SSMIS. [Available from https://cimss.ssec.wisc.edu/itwg/itsc/itsc19/program/papers/10_03_booton.pdf]

Bormann, N., A. Fouilloux, and W. Bell, 2013: Evaluation and assimilation of ATMS data in the ECMWF system. *J. Geophys. Res.*, **118**(23), 12 970–12 980, https://doi.org/10.1002/2013JD020325.

Brogniez, H., and Coauthors, 2016: A review of sources of systematic errors and uncertainties in observations and simulations at 183 GHz. *Atmospheric Measurement Techniques*, **9**(5), 2207–2221, https://doi.org/10.5194/amt-9-2207-2016.

Burgdorf, M., S. A. Buehler, T. Lang, S. Michel, and I. Hans, 2016: The moon as a photometric calibration standard for microwave sensors. *Atmospheric Measurement Techniques*, **9**, 3467–3475, https://doi.org/10.5194/amt-9-3467-2016.

Calbet, X., and Coauthors, 2018: Can turbulence within the field of view cause significant biases in radiative transfer modelling at the 183 GHz band? Atmospheric Measurement Techniques Discussions, doi: 10.5194/amt-2018-181.

Cao, C. Y., M. Weinreb, and H. Xu, 2004: Predicting simultaneous nadir overpasses among polar-orbiting meteorological satellites for the intersatellite calibration of radiometers. *J. Atmos. Oceanic Technol*, **21**, 537–542, https://doi.org/10.1175/1520-0426(2004)021<0537:PSNOAP>2.0.CO;2.

Carminati, F., J. Goddard, H. Lawrence, and S. Newman, 2017: Calibration/Validation Study of GPM GMI. Available from http://www.gaia-clim.eu/system/files/document/d4.6.pdf.

Carminati, F., B. Candy, W. Bell, and N. Atkinson, 2018: Assessment and assimilation of FY-3 humidity sounders and imager in the UK Met Office global model. *Adv. Atmos. Sci.*, **35**(8), 942–954, https://doi.org/10.1007/s00376-018-7266-8.

Chen, K. Y., S. English, N. Bormann, and J. Zhu, 2015: Assessment of FY-3A and FY-3B MWHS observations. *Wea. Forecasting*, **30**, 1280–1290, https://doi.org/10.1175/WAF-D-15-0025.1.

Chen, K. Y., N. Bormann, S. English, and J. Zhu, 2018: Assimilation of Fengyun-3B satellite microwave humidity sounder

data over land. *Adv. Atmos. Sci.*, **35**(3), 268–275, https://doi.org/10.1007/s00376-017-7088-0.

English, S. J., J. R. Eyre, and J. A. Smith, 1999: A cloud-detection scheme for use with satellite sounding radiances in the context of data assimilation for numerical weather prediction. *Quart. J. Roy. Meteorol. Soc.*, **125**(559), 2359–2378, https://doi.org/10.1002/qj.49712555902.

English, S. J., R. J. Renshaw, P. C. Dibben, A. J. Smith, P. J. Rayer, C. Poulsen, F. W. Saunders, and J. R. Eyre, 2000: A comparison of the impact of TOVS arid ATOVS satellite sounding data on the accuracy of numerical weather forecasts. *Quart. J. Roy. Meteorol. Soc.*, **126**, 2911–2931, https://doi.org/10.1002/qj.49712656915.

Geer, A. J., P. Bauer, and N. Bormann, 2010: Solar biases in microwave imager observations assimilated at ECMWF. *IEEE Trans. Geosci. Remote Sens.*, **48**, 2660–2669, https://doi.org/10.1109/TGRS.2010.2040186.

Gu, X. F., and X. D. Tong, 2015: Overview of China earth observation satellite programs [Space Agencies]. *IEEE Geoscience and Remote Sensing Magazine*, **3**(3), 113–129, doi: 10.1109/MGRS.2015.2467172.

Guo, Y., J. Y. He, S. Y. Gu, and N. M. Lu, 2019: Calibration and validation of Feng Yun-3-D microwave humidity sounder Ⅱ. *IEEE Geoscience and Remote Sensing Letters*, doi: 10.1109/LGRS.2019.2957403.

He, J. Y., S. W. Zhang, and Z. Z. Wang, 2015: Advanced microwave atmospheric sounder (AMAS) channel specifications and T/V calibration results on FY-3C satellite. *IEEE Trans. Geosci. Remote Sens.*, **53**(1), 481–493, https://doi.org/10.1109/TGRS.2014.2324173.

Joo, S., J. Eyre, and R. Marriott, 2013: The impact of MetOp and other satellite data within the met office global NWP system using an adjoint-based sensitivity method. *Mon. Wea. Rev.*, **141**, 3331–3342, https://doi.org/10.1175/MWR-D-12-00232.1.

Kazumori, M., and S. J. English, 2015: Use of the ocean surface wind direction signal in microwave radiance assimilation. *Quart. J. Roy. Meteorol. Soc.*, **141**, 1354–1375, https://doi.org/10.1002/qj.2445.

Kazumori, M., A. J. Geer, and S. J. English, 2016: Effects of all-sky assimilation of GCOM-W/AMSR2 radiances in the ECMWF numerical weather prediction system. *Quart. J. Roy. Meteorol. Soc.*, **142**, 721–737, https://doi.org/10.1002/qj.2669.

Lawrence, H., and Coauthors, 2017: An Evaluation of FY-3C MWRI and Assessment of the Long-Term Quality of FY-3C MWHS-2 at ECMWF and the Met Office. European Centre for Medium-Range Weather Forecasts. [Available from https://www.ecmwf.int/sites/default/files/elibrary/2017/17206-evaluation-fy-3c-mwri-and-assessment-long-term-quality-fy-3c-mwhs-2-ecmwf-and-met-office.pdf]

Lawrence, H., N. Bormann, A. J. Geer, Q. F. Lu, and S. J. English, 2018: Evaluation and assimilation of the microwave sounder MWHS-2 onboard FY-3C in the ECMWF numerical weather prediction system. *IEEE Trans. Geosci. Remote Sens.*, **56**(6), 3333–3349, https://doi.org/10.1109/TGRS.2018.2798292.

Li, J., and G. Q. Liu, 2016: Direct assimilation of Chinese FY-3C microwave temperature sounder-2 radiances in the global GRAPES system. *Atmospheric Measurement Techniques*, **9**, 3095–3113, https://doi.org/10.5194/amt-9-3095-2016.

Li, J., Z. K. Qin, and G. Q. Liu, 2016: A new generation of

Chinese FY-3C microwave sounding measurements and the initial assessments of its observations. *Int. J. Remote Sens.*, **37**, 4035–4058, https://doi.org/10.1080/01431161.2016.1207260.

Lorenc, A. C., and Coauthors, 2000: The Met. office global three-dimensional variational data assimilation scheme. *Quart. J. Roy. Meteorol. Soc.*, **126**, 2991–3012, https://doi.org/10.1002/qj.49712657002.

Lu, Q. F., H. Lawrence, N. Bormann, S. English, K. Lean, N. Atkinson, W. Bell, and F. Carminati, 2015: An Evaluation of FY-3C Satellite Data Quality at ECMWF and the Met Office, European Centre for Medium-Range Weather Forecasts. Available from https://www.ecmwf.int/sites/default/files/elibrary/2015/14692-evaluation-fy-3c-satellite-data-quality-ecmwf-and-met-office.pdf.

Macelloni, G., M. Brogioni, P. Pampaloni, A. Cagnati, and M. R. Drinkwater, 2006: DOMEX 2004: An experimental campaign at Dome-C Antarctica for the calibration of spaceborne low-frequency microwave radiometers. *IEEE Trans. Geosci. Remote Sens.*, **44**(10), 2642–2653, https://doi.org/10.1109/TGRS.2006.882801.

Moradi, I., R. R. Ferraro, P. Eriksson, and F. Z. Weng, 2015: Inter-calibration and validation of observations from ATMS and SAPHIR microwave sounders. *IEEE Trans. Geosci. Remote Sens.*, **53**, 5915–5925, https://doi.org/10.1109/TGRS.2015.2427165.

Newell, D., and Coauthors, 2014: GPM microwave imager key performance and calibration results. *Proc. 2014 IEEE Geoscience and Remote Sensing Symposium*, Quebec City, IEEE, 3754–3757, doi: 10.1109/IGARSS.2014.6947300.

Newman, S., F. Carminati, H. Lawrence, N. Bormann, K. Salonen, and W. Bell, 2020: Assessment of new satellite missions within the framework of numerical weather prediction. *Remote Sensing*, **12**, 1580, https://doi.org/10.3390/rs12101580.

Pielke, R., Jr., and R. E. Carbone, 2002: Weather impacts, forecasts, and policy: An integrated perspective. *Bull. Amer. Meteorol. Soc.*, **83**, 393–406, https://doi.org/10.1175/1520-0477(2002)083<0393:WIFAP>2.3.CO;2.

Rawlins, F., S. P. Ballard, K. J. Bovis, A. M. Clayton, D. Li, G. W. Inverarity, A. C. Lorenc, and T. J. Payne, 2007: The Met Office global four-dimensional variational data assimilation scheme. *Quart. J. Roy. Meteorol. Soc.*, **133**, 347–362, https://doi.org/10.1002/qj.32.

Rodgers, C. D., 2000: *Inverse Methods for Atmospheric Sounding*: *Theory and Practice*. World Scientific Publishing Singapore.

Saunders, R., and Coauthors, 2018: An update on the RTTOV fast radiative transfer model (currently at version 12). *Geosci. Model Dev*. Discuss., doi: 10.5194/gmd-2018-64.

Saunders, R. W., T. A. Blackmore, B. Candy, P. N. Francis, and T. J. Hewison, 2013: Monitoring satellite radiance biases using NWP models. *IEEE Trans. Geosci. Remote Sens.*,

51(3), 1124–1138, https://doi.org/10.1109/TGRS.2012.2229283.

Tian, X. X., X. L. Zou, and S. P. Yang, 2018: A limb correction method for the microwave temperature sounder 2 and its applications. *Adv. Atmos. Sci.*, **35**(12), 1547–1552, https://doi.org/10.1007/s00376-018-8092-8.

Uppala, S. M., and Coauthors, 2005: The ERA-40 re-analysis. *Quart. J. Roy. Meteorol. Soc.*, **131**, 2961–3012, https://doi.org/10.1256/qj.04.176.

Wang, X., and X. Li, 2014: Preliminary investigation of Fengyun-3C Microwave Temperature Sounder (MWTS) measurements. *Remote Sensing Letters*, **5**(12), 1002–1011, https://doi.org/10.1080/2150704X.2014.988305.

Wang, Z. Z., J. Y. Li, J. Y. He, S. W. Zhang, S. Y. Gu, Y. Li, Y. Guo, and B. Y. He, 2019: Performance analysis of microwave humidity and temperature sounder onboard the FY-3D satellite from prelaunch multiangle calibration data in thermal/vacuum test. *IEEE Trans. Geosci. Remote Sens.*, **57**, 1664–1683, https://doi.org/10.1109/TGRS.2018.2868324.

Xie, X. X., S. L. Wu, H. X. Xu, W. M. Yu, J. K. He, and S. Y. Gu, 2018: Ascending—descending bias correction of microwave radiation imager on board Fengyun-3C. *IEEE Trans. Geosci. Remote Sens.*, **57**(6), 3126–3134, https://doi.org/10.1109/TGRS.2018.2881094.

Yang, H., and Coauthors, 2011: The Fengyun-3 microwave radiation imager on-orbit verification. *IEEE Trans. Geosci. Remote Sens.*, **49**(11), 4552–4560, https://doi.org/10.1109/TGRS.2011.2148200.

Yang, H., J. Zhou, F. Z. Weng, N. H. Sun, K. Anderson, Q. H. Liu, and E. J. Kim, 2018: Developing vicarious calibration for microwave sounding instruments using lunar radiation. *IEEE Trans. Geosci. Remote Sens.*, **56**(11), 6723–6733, https://doi.org/10.1109/TGRS.2018.2841997.

Yang, J. X., D. S. McKague, and C. S. Ruf, 2016b: Boreal, temperate, and tropical forests as vicarious calibration sites for spaceborne microwave radiometry. *IEEE Trans. Geosci. Remote Sens.*, **54**(2), 1035–1051, https://doi.org/10.1109/TGRS.2015.2472532.

Yang, W. Z., V. O. John, X. P. Zhao, H. Lu, and K. R. Knapp, 2016a: Satellite climate data records: Development, applications, and societal benefits. *Remote Sensing*, **8**, 331, https://doi.org/10.3390/rs8040331.

Zou, C. Z., and W. H. Wang, 2011: Intersatellite calibration of AMSU-A observations for weather and climate applications. *J. Geophys. Res.*, **116**, D23113, https://doi.org/10.1029/2011JD016205.

Zou, X. L., J. Zhao, F. Z. Weng, and Z. K. Qin, 2012: Detection of radio-frequency interference signal over land from FY-3B Microwave Radiation Imager (MWRI). *IEEE Trans. Geosci. Remote Sens.*, **50**(12), 4994–5003, https://doi.org/10.1109/TGRS.2012.2191792.